Hindawi
Mathematical Problems in Engineering
Volume 2020, Article ID 3965980, 12 pages
https://doi.org/10.1155/2020/3965980

Research Article

Experimental and Numerical Study on Characterization and Evaluation of Surface Cracks with Wireless Ultrasonic Sensor

Shuo Chen,[1] Jing Li,[2] Donghui Huang,[3] Yuzhi Chen,[3] and Haitao Zhao[1]

[1]*College of Civil and Transportation Engineering, Hohai University, Nanjing 210000, China*
[2]*Huaihe River Commission of the Ministry of Water Resources, Bengbu 233000, China*
[3]*College of Civil Engineering and Architectural, Jinling Institute of Technology, Nanjing 210000, China*

Correspondence should be addressed to Haitao Zhao; zhaoht@hhu.edu.cn

Received 29 October 2019; Revised 24 April 2020; Accepted 2 May 2020; Published 31 May 2020

Academic Editor: Roberto G. Citarella

Adopting both wireless ultrasonic sensing and numerical simulation techniques, this research investigates the interaction between Rayleigh wave and artificial surface cracks of varying depths. When analyzing experimental ultrasonic data collected by a wireless sensing node, the signals are enhanced through a two-step procedure including signal reconstruction and envelope extraction. The waveforms are interpreted in detail by analyzing wave components through time-of-flight technique. A finite element (FE) model is devised to properly simulate the experimental testing. The simulated waveforms are consistent with experimental results and corroborate the analysis and explanations of experimental waveforms. Based on both experimental and numerical waveform analysis, a relationship between ultrasonic characteristic parameter and crack size is established for the quantitative estimation purpose. The proposed model shows a good agreement with data from both test and literatures.

1. Introduction

The service life of major civil engineering structures can range from decades to hundreds of years. During this period, adverse effects, such as environmental erosion, material aging, and long-term loading effect, can lead to accumulation of damage and structural deterioration [1–3]. Under extreme circumstances, unexpected failure of aging and deteriorating infrastructures can threat public safety. In order to prevent such catastrophes, real-time information on structural condition should be collected. To this end, numerous structural sensing techniques have been developed and studied.

Among various techniques, nondestructive testing (NDT) has been widely used in practice. NDT technique can reveal both internal and surface defects without introducing further damage to the structure and usually with little interruption to the normal operation. Correlated with changes of different physical phenomena (e.g., pressure, heat, and scattering of elastic waves), NDT can provide valuable data for evaluating structural integrity, safety, and reliability. Among different NDT methods, Rayleigh wave-based ultrasonic testing method is particularly suited for detecting the presence, orientation, distribution, and geometric shape of surface cracks. A primary advantage of the Rayleigh wave is that during propagation it suffers less spatial attenuation than body waves. Most energy of Rayleigh wave propagates within a wavelength from the free surface of a tested specimen [4]. Moreover, Rayleigh wave is sensitive to the surface defects with a depth less than a few times of the wavelength [5]. The Rayleigh wave velocity is constant in the same medium, and the wavelength is only related to frequency. Therefore, the detection depth can be easily controlled by varying the frequency of the wave. Because of all the features mentioned above, Rayleigh wave is ideal for nondestructive evaluation with low-power wireless sensing devices.

However, because the interaction mechanism between Rayleigh wave and crack is not yet fully understood, the detection and sizing of surface cracks with Rayleigh wave is still a research subject of great interest. A number of experimental research studies on this topic have been reported.

Viktorov [4] observed a scattering phenomenon of Rayleigh wave at a notch in an aluminum bar and proposed a crack size estimation method involving reflection and transmission coefficients. After calculation, he also pointed out that there was a loss of complementarity between the two coefficients due to the conversion and energy loss at the interface near the notch. On the basis of Viktorov's work, Domarkas et al. [6] studied the scattering from surface cracks at a fixed incidence angle with Rayleigh waves of different frequencies. They explained the variation of reflection coefficient as resonances at the crack and used it for crack dimension estimation with a satisfactory precision. Rokhlin and Kim [7] conducted a detailed experimental study of scattering of Rayleigh waves at pit-induced cracks in an AI2024-3 steel plate. They studied the reflected waveforms under the influences of crack depths and tension step-up loads, compared the experimental data with theoretical results, and explored the potential application for crack sizing in a fatigue test. Hernandez-Valle et al. [8] adopted laser-induced Rayleigh wave for studying branched defects in aluminum samples. Branch was added to a slot to simulate stress corrosion defects, and a connection was successfully established between characteristics of collected signals and the geometry of cracks by amplitude and frequency spectrum analysis.

In parallel to experimental study on the interaction between Rayleigh wave and surface defects, a great number of articles have also been published on aspects of theoretical modeling and numerical simulations. Comparing experimental studies, theoretical and numerical research can provide detailed motion prediction of all particles in the body, providing guidance towards improving future experiments and data analysis. For example, Kino [9] and Auld [10] derived mathematical formula by reciprocity theorem, which could be used to calculate the transmission coefficient from one transducer to another through an arbitrarily shaped flaw. Achenbach and Gautesen [11] extended geometrical theory of diffraction from the optics research to investigate the diffraction of elastic waves by a crack. They study detailed the propagation process from the source to the receiver through a crack and successfully formulated the characteristic interference pattern of diffracted wave using both frequency and angle. Valle et al. [12] established a finite element (FE) model to simulate the propagation of guided circular wave in a cracked hollow cylinder. They showed the feasibility to accurately size and locate a radial crack by analyzing simulated results using Auld's formula and time-frequency representations. Rosli et al. [13] performed another study on detecting surface-breaking defects of a wide range of depths and angles. They built a 2D FE model to simulate Rayleigh wave interactions and revealed the trends that transmission coefficients vary with different geometric parameters of defects, which agreed well with experimental results.

Traditional cabled equipment for Rayleigh wave testing is usually bulky, expensive, and inconvenient to deploy in the field. The equipment is better suited for short-term inspection than long-term deployment in the field. As reported by Straser and Kiremidjian [14], for a general bridge testing system, cable installation can take up to 75% of total time and 25% of total cost. On the contrary, wireless smart sensors with attractive characteristics, such as compactness, ability of wireless data transmission, low cost, power efficiency, and on-board processing capabilities [15], can be a promising alternative to traditional cabled equipment. The compact size and wireless communication make deployment much more convenient in the field. The low-cost attribute makes it feasible and economical to deploy a dense array of sensors on a civil structure, significantly increasing the capability for accurate damage localization. On-board processing feature enables computation of damage-sensitive parameters in real time, immediately upon data collection. Designed with these characteristics, Martlet is a wireless sensing platform codeveloped by the University of Michigan, Georgia Institute of Technology and Michigan Technological University [16]. Martlet adopts a dual-core Texas Instruments processor with a hardware floating-point unit, which supports high-speed data acquisition at up to 3 MHz sample rate. It also incorporates an extensible platform to support heterogeneous sensing for both global- and local-based damage detection. A customized daughter board was designed for ultrasonic measurement and integrated with the Martlet mother board to compose a wireless ultrasonic sensing node. Architectural design and a preliminary performance validation of the wireless ultrasonic sensing node was illustrated thoroughly in a preceding article [17].

This paper aims to investigate the interaction of Rayleigh wave with artificial surface cracks of varying depths, through both wireless sensing experiments and FE analyses. The rest of the paper is organized as follows. Section 2 illustrates the experimental setup for the ultrasonic measurement using a wireless sensing node. In Section 3, proper selection of key parameters (e.g., material properties, excitation wave generation, meshing size, time step, and boundary condition) is discussed through finite element modeling and correlating simulation with experimental results. Section 4 provides analysis and comparison of Rayleigh wave scattering from the perspective of waveform and transmission coefficients. The study will help improve quantitative size estimation of surface defects and ultrasonic waveform analysis in future fatigue crack detection. Section 5 presents the summary and conclusions.

2. Experimental Setup

The wireless ultrasonic sensing node consists of a Martlet mother board and an ultrasonic daughter board that can be plugged-in on top (Figure 1). A detailed description of the hardware architecture has been previously reported [17] and thus will not be repeated herein. In short, the ultrasonic daughter board contains modules for both ultrasonic signal excitation and signal receiving. The wireless ultrasonic sensing node can perform signal conditioning to the received ultrasonic signal prior to digitization. The excitation module generates a series of square wave bursts at 500 kHz with peak-to-peak amplitude up to 40 V (an amplitude of 18 V is used in this study). In the receiving module, a band-pass filter and an amplifier are used to increase the

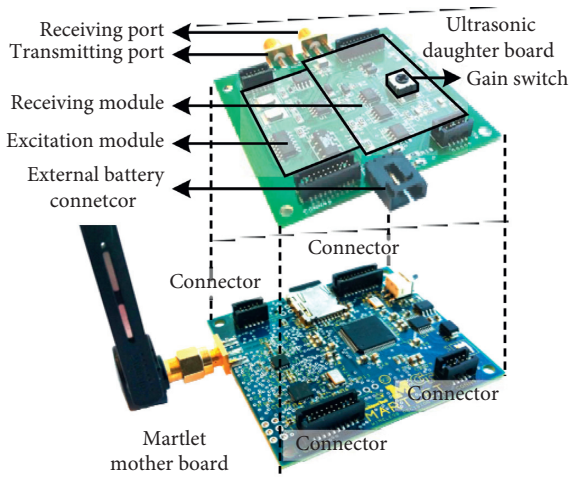

Figure 1: Schematic diagram of the ultrasonic daughter board stacking on the Martlet mother board.

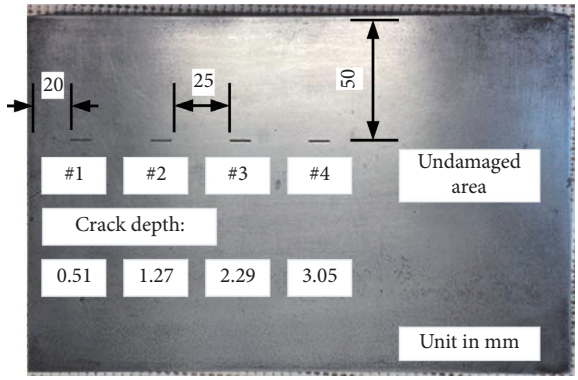

Figure 2: Steel specimen (241.3 mm × 152.4 mm × 25.4 mm) with four artificial cracks of different depths.

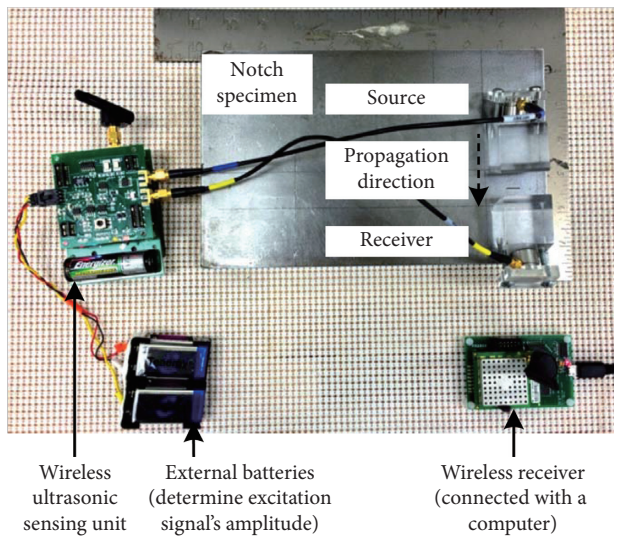

Figure 3: Experimental setup for wireless ultrasonic test.

signal-to-noise ratio of the received ultrasonic signal. Considering the frequency of interest is around 500 kHz, the high-pass and low-pass cutoff frequencies are set at 159 Hz and 2 MHz, respectively, to suppress background noise while avoiding waveform distortion. In addition, the gain for output signal amplification is selectable among 10 dB, 20 dB, and 30 dB using a rotary switch on the ultrasonic daughter board (30 dB by default in the experiment). The accuracy of the generation and recording of ultrasonic waveforms are verified by comparing to those generated/received by cabled commercial equipment.

Figure 2 presents the thick steel specimen plate used in this study, which is 241.3 mm × 152.4 mm × 25.4 mm (thickness). Four artificial cracks with different depths (0.51, 1.27, 2.29, and 3.05 mm) were created using an electrical discharge machine to simulate surface cracks with different levels of damage (depths). The artificial cracks have the same length of 9.3 mm and opening width of 0.58 mm. The distances between adjacent artificial cracks are about 25 mm.

The experimental setup is shown schematically in Figure 3. The ultrasonic measurements were performed using a pair of ultrasonic transducers (Model: WC50-0.5, Ultran Group) with a central frequency of 500 kHz. Each transducer was attached to a Plexiglas wedge for Rayleigh wave generation and detection separately, and the distance between the source and receiver is 25.4 mm in a typical pitch-catch arrangement. Light lubrication oil was used as acoustic couplant at the interfaces between transducer/wedge and wedge/specimen surfaces. When the experiment begins, the server wakes up the wireless ultrasonic sensing node that commands the ultrasonic daughter board. The ultrasonic daughter board then generates five cycles of 18 V and 500 kHz square wave at every burst and repeats the same bursts every 260 μs. The bursts are fed into the transmitting ultrasonic transducer to launch Rayleigh waves in the specimen. Consequently, the propagating waves are detected by the receiving ultrasonic transducer, and the ultrasonic signals are collected by the signal receiving module in the ultrasonic daughter board. After filtering and amplifying, analog output signals are digitized at a sampling rate 2 MHz. The digitized data of the received ultrasonic signal can be wirelessly transferred to the server. Using the amplitude of the received Rayleigh wave, which propagated through the artificial crack, it is expected to distinguish the depth of each artificial crack. Before reviewing the experimental results, the next section first describes finite element modeling that attempts to simulate this ultrasonic testing.

3. Finite Element Modelling

Rayleigh wave has perpendicular and parallel components, which indicates it is a two-dimensional propagation wave [4]. In the material with characteristics of homogeneous, isotropic, and linearly elastic (e.g., steel in this paper), the interaction of plane Rayleigh wave in a steel specimen with an artificial crack can be analyzed using a two-dimensional model [18], as presented in Figure 4. The established FE model attempts to simulate the experimental testing by characterizing the interaction between Rayleigh wave and artificial cracks under the plane-strain condition. To fulfill this end, PLANE42 element is adopted in commercial

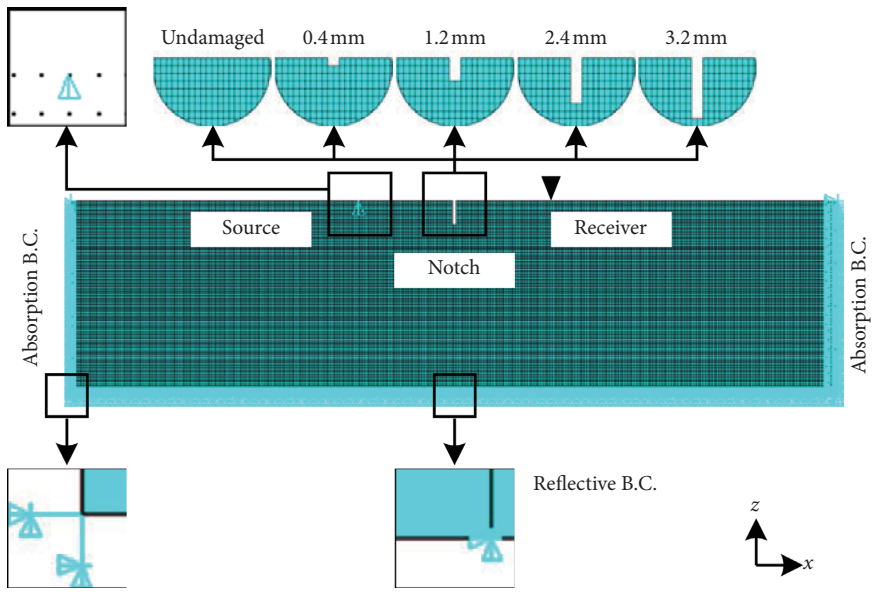

Figure 4: Two-dimensional FE model of a steel plate with one artificial crack on top.

software ANSYS, which is a plane element and defined by four nodes each with translation along both x and z directions. As shown in Figure 4, artificial cracks have a rectangular shape with different depths and their surfaces have stress-free boundary conditions. The height of the FE model is the same as the specimen thickness (25.2 mm). Considering both be consistent with the experiment and convenience for modeling, the length of the model is taken to be 100.8 mm. The coordinate origin of the model is set at the bottom center, and the coordinate orientations are shown in Figure 4 as well.

3.1. Material Properties and Excitation Signal Generation. Since the material properties have a significant influence on the simulation results [19], they should be chosen as close as possible to the actual properties of the specimen. According to the handbook published by American Society of Metals [20], the density, elastic modulus, and Poisson's ratio of simulated steel material are 7.85×10^3 kg/m^3, 200 GPa, and 0.24, respectively. Moreover, considering reference data provided in literature [21] and a measurement carried out with a specimen of similar material [22], the propagation velocities of compression, shear, and Rayleigh waves in the model are selected as 5900 m/s, 3200 m/s, and 2989 m/s, respectively.

The excitation signal is generated at the position labeled as "source" in Figure 4, and the surface distance from the source to the artificial crack center is 12.7 mm. Two approaches are frequently used to shape waveforms of excitation signals. One is to approximately apply a time-varying force waveform at the "source" FE node based on a certain function (e.g. half-sine function) [23]. The other is to specify the displacement waveform of the "source" node and generate a displacement record closely matching the motion equation of Rayleigh wave in homogeneous elastic materials. The actual motion that occurs in an experimental testing is subject to the electromechanical coupling and sensitivity coefficients of the particular ultrasonic transducer used in the experiment. To identify an appropriate waveform that models the motion of "source" node, Treeby et al. [24] applied a semisinusoidal window to a series of sinusoidal signals to generate a tone-burst. They compared the simulated wave with the theoretical solution in both time and frequency domains and demonstrated the high accuracy. In this paper, the second approach is adopted to generate the excitation signal, and the waveform of a five-cycle 500 kHz tone-burst with normalized amplitude is presented in Figure 5.

3.2. Finite Element Meshing. Meshing size in finite element modeling can significantly influence simulation accuracy, which is affected by the wavelength and frequency of interest. According to Mirahmadi and Honarvar [25], the maximum meshing size should be less than 1/10 of the shortest propagating wavelength. For a 500 kHz Rayleigh wave, the smallest wavelength is approximately 5.98 mm; thus, the maximum element size should be less than 0.598 mm. In addition, Valliappan and Murti [26] provided another empirical equation to estimate the element size g:

$$g \leq \zeta \frac{V_s}{f}, \tag{1}$$

where ζ is an empiric constant related to material properties, which takes a value of 0.25 for homogeneous materials; V_s is the shear wave velocity; and f is the maximum Rayleigh wave frequency of interest. By equation (1) and material properties discussed in Section 3.1, the maximum element size is calculated and should be smaller than 1.6 mm.

Considering the calculations above, the element sizes along x- and z-axis are set at 0.3 mm and 0.4 mm in this study. As a result, the undamaged FE model has 21,424 elements and 21,888 nodes, and the number is reduced by 2–18 for a model with an artificial crack of varying depth.

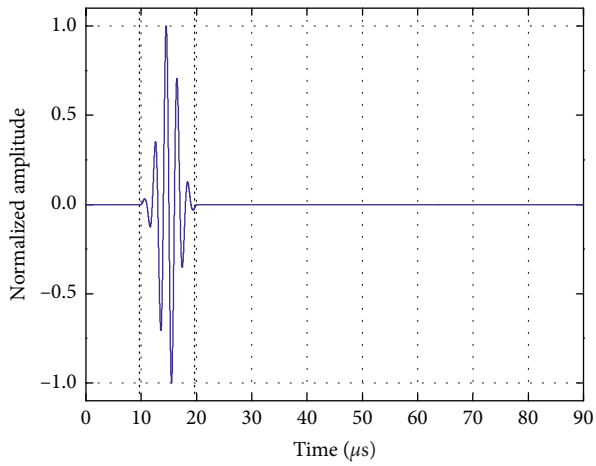

Figure 5: Normalized five-cycle burst of 500 kHz center frequency for excitation.

3.3. Boundary Conditions. In the FE model, the nodes at the specimen bottom are fixed in both vertical and horizontal directions. Due to sufficient spacing between the artificial cracks and the boundaries of the test specimen, it should experience little interference from boundaries or a neighboring artificial crack. Therefore, the wave can be modeled as propagating indefinitely along both positive and negative directions of x-axis. To achieve this effect in the FE model, an artificial boundary is set to offset the impact caused by the left and right boundaries. In this paper, artificial boundaries with viscous springs are adopted along the x-axis as the absorbing boundary condition ("Absorbing B. C." in Figure 4) for its simplicity, stability, and effectiveness [27]. By adding linear spring and damper elements along both horizontal and vertical directions at the nodes on an absorbing boundary, most of the propagating energy is absorbed to minimize reflection from these boundaries. The stiffness coefficient for the springs and the damping coefficient for the dampers are calculated as follows [28]:

$$\begin{cases} K_x = \alpha_x \left(\dfrac{G}{R}\right), \\ K_z = \alpha_z \left(\dfrac{G}{R}\right), \\ C_x = \rho V_{\mathrm{p}}, \\ C_z = \rho V_{\mathrm{s}}, \end{cases} \tag{2}$$

where K_x and K_z are stiffness coefficients along x and z directions, separately; α_x and α_z denote empirical artificial boundary parameters, which are set at 1.0 and 0.5 according to the recommendation [29]; G represents shear modulus of the material; R is the distance between the source and the boundary; C_x and C_z are damping coefficients along x- and z-axis, respectively; ρ denotes the medium density; and V_{p} is the compression wave velocity.

3.4. Simulation Time Step. The selection of time step should take into account both numerical accuracy and computing time. An empirical formula was given by Valliappan and Murti [26]:

$$\tau \leq \frac{g}{V_{\mathrm{p}}}, \tag{3}$$

where τ represents the time step and g is the element size calculated from equation (1). As a result, the time step should be smaller than 0.27 μs. In order to be comparable with experimental results, the time step is set at 0.1 μs in our simulation. Based on the experimental data [30], the collected signal fades away in about 90 μs, and the total number of simulated time steps is determined as 900.

4. Quantitative Assessment of Surface Crack Size

4.1. Data Processing Approaches for the Wireless Ultrasonic Data. The sampling frequency used in the experiments was 2 MHz. Because the central frequency of the ultrasonic signal was at around 500 kHz, 4 data points were sampled for every cycle of the ultrasonic signal. Although the sampling frequency is relatively low, it meets the requirement of Nyquist-Shannon sampling theorem [31, 32]. Signal reconstruction using upsampling and the cardinal sine function (a.k.a. sinc function) can be carried out to restore most of the details in the band-limited ultrasonic waveform [33]:

$$x_{\mathrm{re}}(t) = \sum_{i=1}^{n} x[i] \cdot \sin c\left(t f_{\mathrm{s}} - (i-1)\right), \tag{4}$$

where $x_{\mathrm{re}}(t)$ is the reconstructed and upsampled signal; t represents time; $x[i]$ is the i^{th} sampled data point in the wireless ultrasonic data; n denotes the total number of data points; f_{s} is the wireless sampling frequency.

During the measurement, a slight dislocation of the transducer positions causes change in the received signal with a different waveform and different local amplitudes. The solid and dashed curves in Figure 6 illustrate two collected signals for which the receiving transducer position is slightly disturbed. This phenomenon can affect peak amplitude determination, which, in turn, causes an error in artificial crack size estimation. In order to reduce the effect of transducer positions, an envelope detection process using discrete Hilbert transform is performed. The theoretical derivation of the algorithm was presented in a previous paper [17]. Generally, the envelope of an upsampled signal can be extracted using

$$x_{\mathrm{re}}^{\mathrm{env}}(t) = \sqrt{x_{\mathrm{re}}^2(t) + \overline{x_{\mathrm{re}}(t)}^2}, \tag{5}$$

where $x_{\mathrm{re}}^{\mathrm{env}}(t)$ is the corresponding envelope curve for a collected signal $x_{\mathrm{re}}(t)$ and $\overline{x_{\mathrm{re}}(t)}$ denotes the Hilbert transform of $x_{\mathrm{re}}(t)$, which can be obtained through a series of calculations involving convolution and Fourier transform. The solid curve in Figure 6 shows the envelopes of the two collected signals overlap.

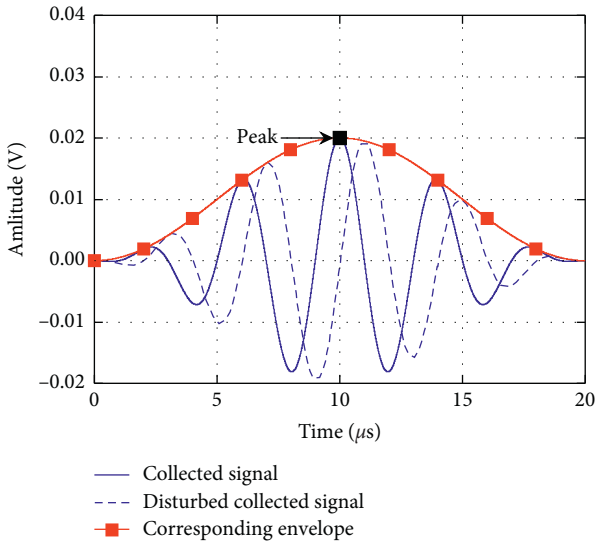

Figure 6: Diagram for two modulated signals with the same envelope waveform.

4.2. Characterization of Wireless Ultrasonic Data. The wireless data with a sampling frequency of 2 MHz were upsampled to 10 MHz with the algorithm proposed in the preceding section. The validation of the algorithm was conducted by a comparison between the upsampled wireless sensing signals and corresponding signals collected from commercial cabled equipment at same sampling frequency. Detailed analysis was reported in the earlier paper [17]. Figures 7(a)–7(e) show the ultrasonic waveforms and corresponding envelope curves, for each of the undamaged case and four artificial crack cases. The waveform fluctuates very little after 70 μs, and for ease of comparison between experimental and simulation waveforms in the following section, the gain of the collected signals (30 dB) is removed.

Using the propagation velocities of compression, shear, and Rayleigh waves discussed in Section 3.1, the propagation distance difference between waveforms of different arrival times can be calculated. Based on geometric analysis, the causes of waveforms at different arrival times can then be deduced. Therefore, relative arrival times of different wave components are crucial in this study, while absolute arrival time is irrelevant. For comparison, in Figures 7(a)–7(e), all waveforms are time-aligned so that the first arriving peak with a significant positive amplitude is at around 10 μs.

In these figures, a very similar waveform trend can be observed. The first group of waves arrives approximately between 8 and 20 μs, which means the propagation distance is the shortest. The first waves packet contains the highest peak, and its amplitude decreases significantly for larger artificial crack depths. Since the amplitude has a positive correlation with energy, the first arriving component has the highest percentage of the total energy. Considering this component has the features of shortest propagation distance and the highest share of energy, based on Pertsch et al. [34], the first arrival can be attributed to transmitted Rayleigh wave, which travels along the horizontal surface and the edge of the artificial crack. It is marked as path #1 in Figure 7(f), and its propagation distance is the straight-line distance between two sensors, which is 25.4 mm.

The second group of waves arrives between approximately 20 and 30 μs. Based on the arriving time difference from path #1, the additional propagation distance should be about 29.89 mm (for Rayleigh wave) or 32 mm (for shear wave). Therefore, the total propagation distance of the second group of waves is between 55.29 mm and 57.4 mm. Based on geometry relationship, the distance for a wave traveling from the source to the receiver through a single bottom reflection (path #2 in Figure 7(f)) is 56.80 mm, which confirms the second group to be bottom reflection waves. In addition, its amplitude is low and the arriving time slightly lengthens as the artificial crack depth increases. These features match the description of creeping waves reported in literature [35]; thus the waves propagating through paths #3 and #4 in Figure 7(f) may also contribute to the formation of second group of waves.

The third group of waves arrives at approximately 30 μs. Following the procedures of time-difference analysis used previously, the traveling distance for these waves is around 100.13 mm. Considering the distance for one propagation is around 56 mm, the third group of waves is likely the double reflection shear waves (path #5 in Figure 7(f)). In addition, Pertsch [18] pointed out that a wave with a delay of 25 μs exists in the excitation signal, due to the reflection inside the wedge with identical dimensions. Therefore, this "delayed" excitation signal travels through path #1 and should reach the receiver at around 35 μs. Therefore, it can also contribute to the formation of third group of waves. The full route of this delayed wave should be a combination of paths #6 and #1 in Figure 7(f).

Last but not least, the fourth group of waves arrives at approximately 45 μs, and the arriving time varies with the depth of the artificial crack. Based on the different arrival times, the propagation distances are roughly between 130 mm and 160 mm and match the geometric distance of a triple reflection. Since this group of waves helps little in the artificial crack size estimation, the origin of the fourth-arriving waveform will not be discussed in detail in this paper.

4.3. FEM Simulation of the Interaction between Surface Acoustic Wave and a Crack. A proper FE model should not only accurately reflect experimental conditions, but also provide simulation results that are close to experimental data. To validate the FE simulation, both undamaged and damaged scenarios are adopted. Figure 8(a) compares the simulation result (solid line with circular markers) and a set of reconstructed wireless sensing data (solid line) for the undamaged scenario; Figures 8(b)–8(e) provide the comparison for the artificial cracks with depths of 0.40 mm, 1.27 mm, 2.29 mm, and 3.05 mm, respectively.

In Figures 8(a)–8(e), the experimental waveforms are upsampled and reconstructed as described in the previous

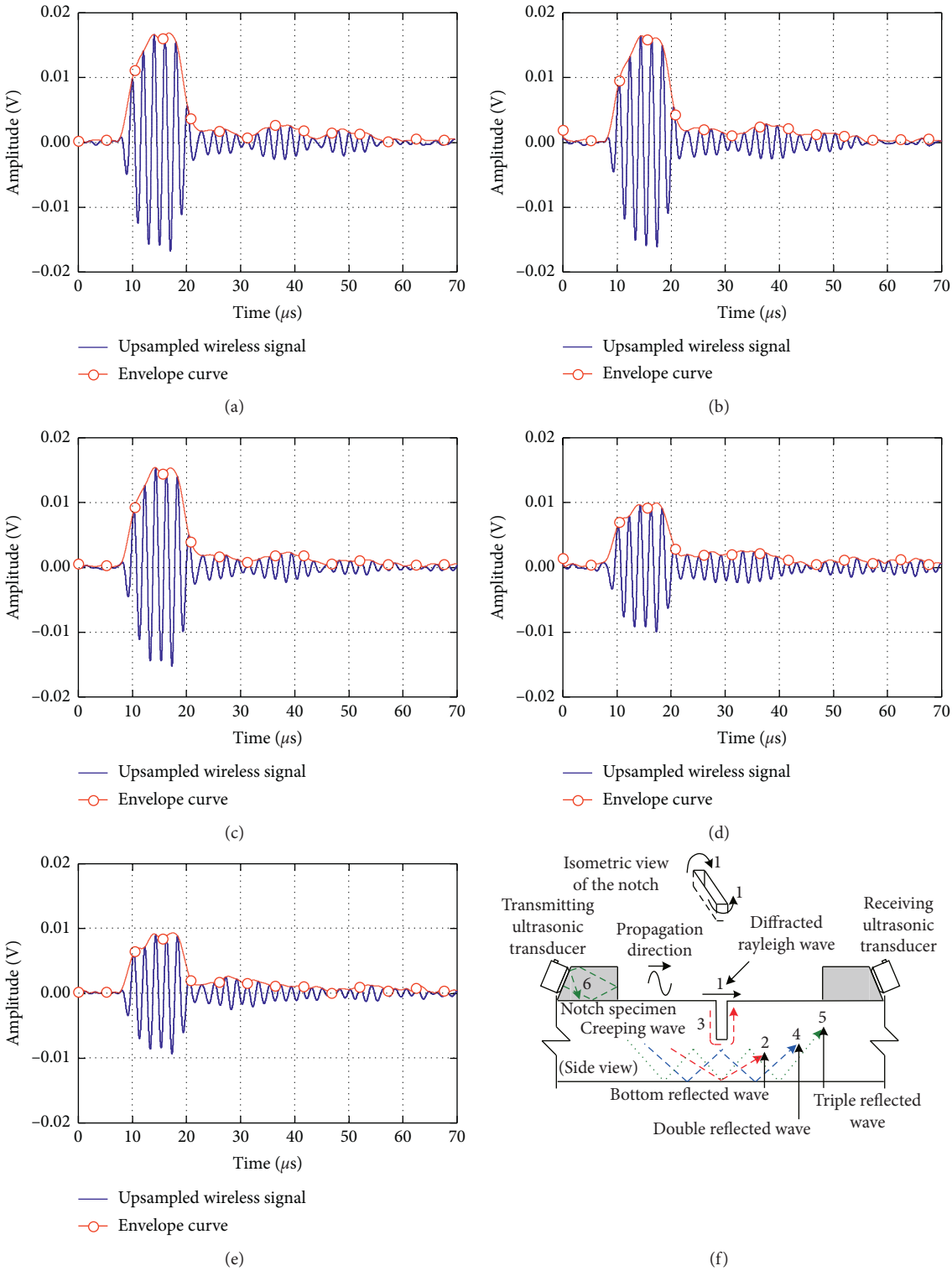

Figure 7: Wireless ultrasonic data and envelopes. (a–e) Wireless signal and envelope obtained from undamaged area and artificial cracks with depths of 0.51 mm, 1.27 mm, 2.29 mm, and 3.05 mm, respectively. (f) Diagram for different possible propagation path.

section. For simulated waveforms, time-varying displacements are converted to voltage based on electromechanical coupling and sensitivity coefficients of the WC50-0.5 ultrasonic transducer. After time-aligning process, the first obvious peak with a positive amplitude is around 10 μs and correlation coefficients and root mean square errors (RMSE) can be calculated. The correlation coefficients decrease slightly. The values are 0.959, 0.916, 0.869, 0.843, and 0.831, respectively. The RMSEs increase firstly, and then decrease. The values are 0.0013 V, 0.0018 V, 0.0021 V,

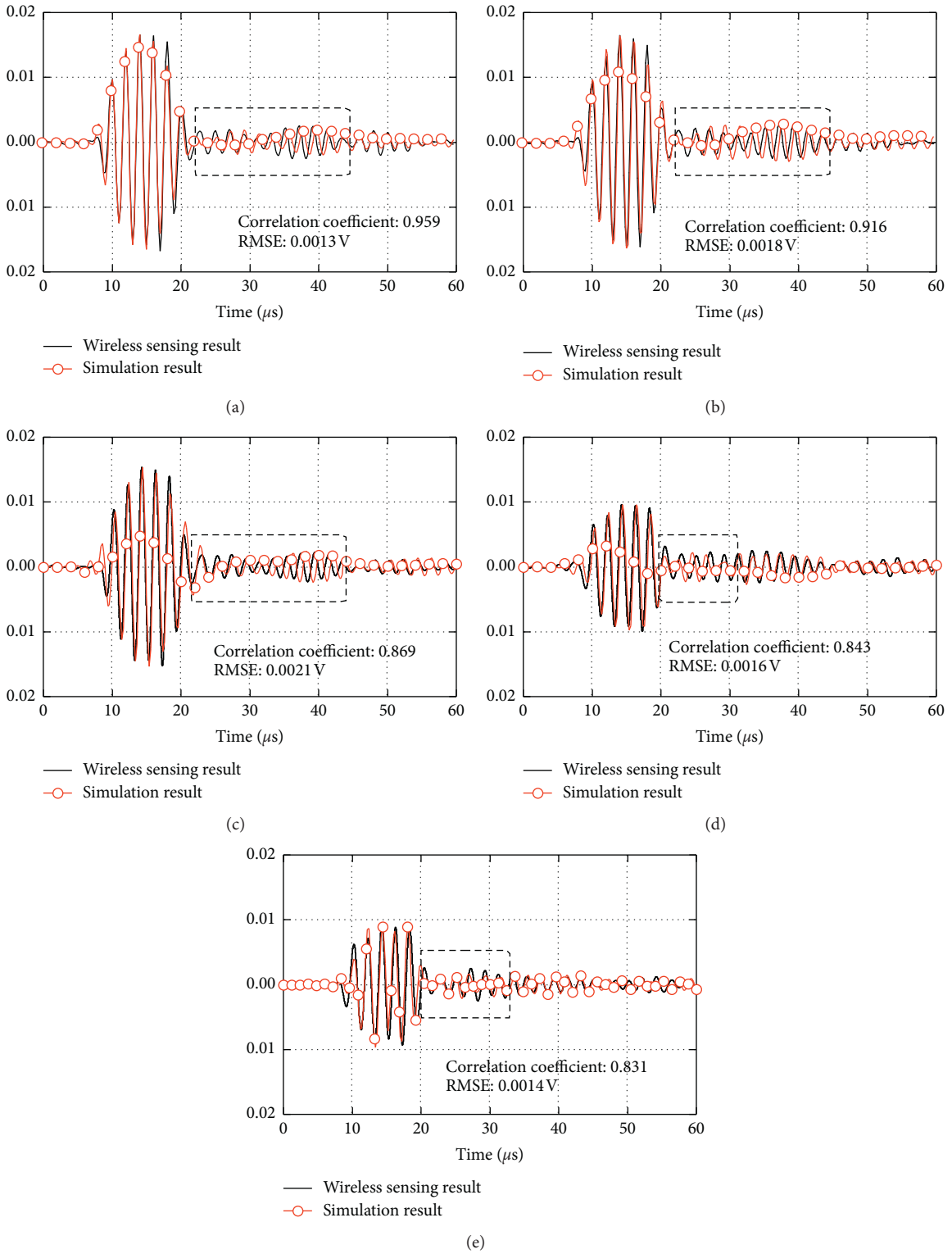

Figure 8: Waveform comparison between experimental and simulation results. (a) Waveform obtained from undamaged scenario. (b–e) Waveform obtained when the depth of artificial crack is 0.40 mm, 1.27 mm, 2.29 mm, and 3.05 mm, respectively.

0.0016 V, and 0.0014 V, respectively. The inversed V-shape trend is the result of a mutual influence of correlation coefficient reduction and decrease of overall amplitude. In the preceding three scenarios, the amplitudes of signals change little, and the variation of correlation coefficient is dominant. For the latter two cases, the factor of amplitude trumps the correlation coefficient, and the significant falling of amplitude leads to a decrease of RMSE. Overall,

considering correlation coefficients are close to 1 and the amplitude of all waveforms is on the order of 0.01 V (much higher than the RMSE values), it can be concluded that the simulations well modeled the experiments. The selected waveform of the excitation signal is also deemed appropriate to simulate the ultrasonic source in the experiment. Hence, the simulation methods established in this study can be used for future analysis of wave interaction, for example, identifying the origin of waveforms with different arrival times.

If the waveforms in the time domain are examined carefully, they can be divided into multiple segments, from which several common features can be observed by comparing the waveforms. Firstly, it can be found that simulation waveforms agree well with the experimental results between 10 and 20 μs. This waveform segment is easily attributed to the Rayleigh wave propagation, based on previous time-of-flight analysis. In the meantime, it can also be observed that there is an approximately 1 μs delay between simulated waveforms and the experimental ones during the 20–40 μs (see dashed boxes in Figure 8). This phenomenon indicates that the velocity of the simulated wave may have a slight difference from the experiment. In the literature [36, 37], it is generally acknowledged that wave velocity is only associated with material properties in a homogeneous linear elastic medium that is strain-/stress-free. Despite the careful selection of material properties, we can reasonably suspect that the minor time difference between simulated and experimental waveform is caused by a small difference between simulated and experimental material properties. Considering the similarity in analysis, scenario of cracks depths at 0.40 mm is selected as the representative for the study of the origin of wave segments with different arrival times.

At the $14^{\text{th}}\mu$s in Figure 8(b), the peak of the transmitted Rayleigh wave passes through the receiver for the 0.40 mm artificial crack. Figure 9(a) shows the simulated wave propagation amplitude at this instant. In the figure, four significant waves can be observed, that is, incident wave, transmitted wave, bottom reflected wave, and artificial crack reflected wave. Among them, the propagation directions of incident and transmitted waves are opposite and are perpendicular to a virtual plane defined by $x = -12.6$ mm (source position). The wave amplitudes are nearly symmetric about this plane, except that the peak amplitude of the transmitted wave is a little lower than that of the incident wave, which is due to the energy loss of the transmitted wave at the artificial crack. In addition, the transmitted wave shows a significant attenuation inside the specimen, which agrees with the feature of a Rayleigh wave. Therefore, the simulation corroborates the conclusion of experimental analysis, in which the first wave group mainly consists of transmitted Rayleigh waves. In addition, the figure shows a bulk wave propagates toward the bottom, gets reflected by the bottom surface, and finally arrives back at the top surface. This bottom reflected wave arrives at the receiver approximately between 20 μs and 30 μs, and its propagation feature matches the description of shear wave in Liu et al. [38]. Consequently, the bottom reflecting shear wave in Figure 9(a) supports the previous time-of-flight analysis of the experimental data collected by the receiver between 20 μs and 30 μs.

Figure 9(b) shows another example instant from the same simulation model as in Figure 9(a). The instant corresponds to the $30^{\text{th}}\mu$s in Figure 8(b), when the incident wave has propagated across the left boundary. From the figure it can be seen that the incident wave fades out and barely leaves any reflected waves. Therefore, it can be concluded that the absorbing B. C. set in this study is functional and can help to minimize the reflection at the boundary. Furthermore, a bottom-surface-bottom reflected wave is shown in Figure 9(b) to reach the receiver around 35 μs after the data collection. The existence of this bottom double reflected wave in the simulation explains the experimental analysis of the wave between 30 and 45 μs in Figure 8(b).

4.4. Transmission Coefficients versus Crack Size. Based on the waveform analysis above, it can be concluded that the first-arrival wave (i.e., transmitted Rayleigh wave) contains most of the energy in a collected signal and can be used to analyze the variation in artificial crack depth. Hence, based on the envelope amplitude of the transmitted Rayleigh wave, a transmission coefficient (T_r) is adopted for artificial crack size assessment and defined as

$$T_r = \frac{A^{\text{env}}}{A^{\text{env}}_{\text{undamaged}}}, \tag{6}$$

where A^{env} is the envelope amplitude of the transmitted Rayleigh wave from an artificial crack and $A^{\text{env}}_{\text{undamaged}}$ is the envelope amplitude of propagated Rayleigh wave collected at the same distance from an undamaged area. The envelope amplitudes are obtained through discrete Hilbert transform as described in Section 4.1.

Figure 10(a) illustrates the compare the experimental transmission coefficients versus normalized artificial crack depths (crack depth/wavelength of the 500 kHz Rayleigh wave) with these available in literature [4, 39–42]. Overall trend from these six studies is shown to match each other. Furthermore, the plot calculated from the wireless sensing data (in this study) is within the bounds provided by the references and close to the ones presented in Hévin et al. [41]. Using the wireless sensing data, a linear regression is performed between normalized crack depth and transmission coefficient, and the result is presented in Figure 10(b). The correlation coefficient and RMSE between experimental data and linear regression curve are 0.963 and 0.069, respectively. These results show that using the transmission coefficient, the linear regression relationship can be used as a preliminary estimate for crack depth under similar testing conditions.

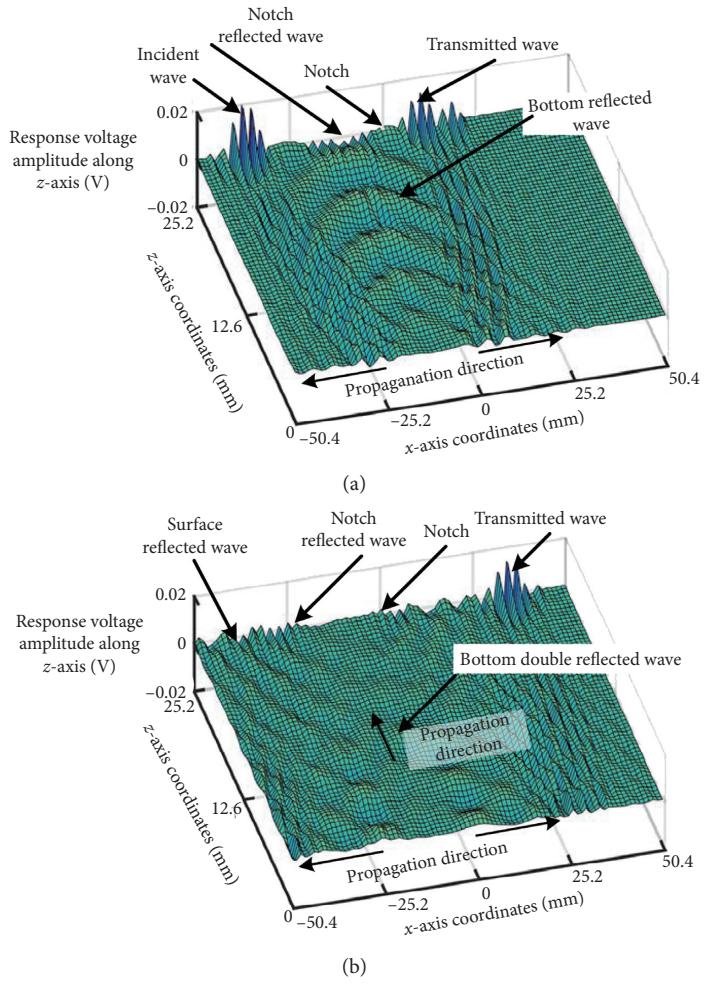

Figure 9: Amplitude of wave propagation with crack depth of 0.40 mm at two instants: (a) $t = 14\,\mu s$ (peak of transmitted signal passes through the receiver); (b) $t = 30\,\mu s$ (incident signal has passes through left boundary).

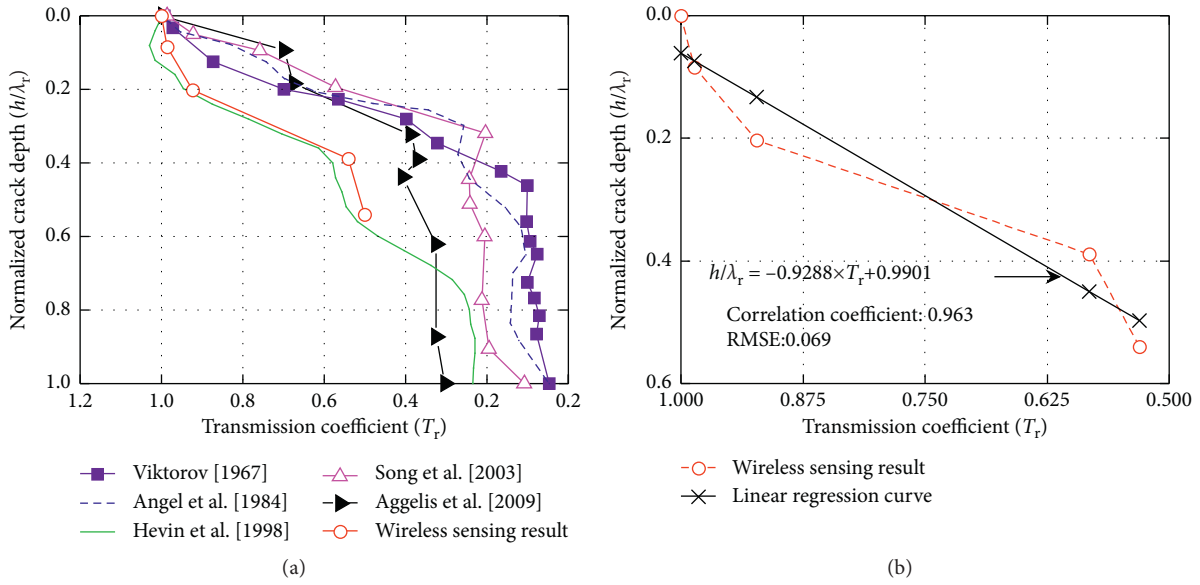

Figure 10: Transmission coefficient versus normalized crack depth: (a) comparison with test results in the literature; (b) experimental results and corresponding linear regression curve.

5. Conclusions

Aiming for the nondestructive quantitative assessment of crack sizes, this paper proposes a study on the interaction between Rayleigh wave and artificial surface cracks of different sizes using both experimental and numerical methods. A self-developed wireless ultrasonic sensing device is adopted for the ultrasonic measurement of surface cracks in a steel plate. In addition, for more effective identification purpose, a set of signal processing procedures is applied to the collected ultrasonic signals. Through wave propagation analysis, wave components with different arrival times are identified and explained. Emulating the experimental setup, an FE model is established. And a careful discussion is conducted on the key parameters, such as simulated material properties, method for Rayleigh wave excitation, finite element mesh size, boundary condition setup, and time step. The simulated waveforms are consistent with experimental results and corroborate the analysis of experimental waveforms. On the basis of analysis, transmission coefficient of the transmitted Rayleigh wave, which is sensitive to crack depth, is adopted to represent crack size. Furthermore, the linear regression results (between crack depth and transmission coefficient) have the potential for future quick estimation of crack depths under similar testing conditions.

Data Availability

All data used to support the findings of this study are available from the corresponding author upon request.

Conflicts of Interest

The authors declare that there are no conflicts of interest regarding the publication of this paper.

Acknowledgments

This work was supported by the China Postdoctoral Science Foundation Funded Project (no. 2018M632217). The authors also gratefully acknowledge the financial support from the National Natural Science Foundation of China under Grant nos. 51908192, 51878245, and 51708265. This research was also sponsored by the Natural Science Foundation of the Higher Education Institutions of Jiangsu Province (no. 16KJB560004) and the Natural Science Foundation of Jiangsu Province (no. BK20160106).

References

[1] V. Berardi and G. Mancusi, "Time-dependent behavior of reinforced polymer concrete columns under eccentric axial loading," *Materials*, vol. 5, no. 11, pp. 2342–2352, 2012.

[2] V. P. Berardi and G. Mancusi, "A mechanical model for predicting the long term behavior of reinforced polymer concretes," *Mechanics Research Communications*, vol. 50, pp. 1–7, 2013.

[3] V. P. Berardi, L. Feo, G. Mancusi, and M. De Piano, "Influence of reinforcement viscous properties on reliability of existing structures strengthened with externally bonded composites," *Composite Structures*, vol. 200, pp. 532–539, 2018.

[4] I. A. Viktorov, *Rayleigh and Lamb Waves: Physical Theory and Applications*, Plenum Press, New York, NY, USA, 1967.

[5] B. A. Auld, "Rayleigh wave propagation," *Rayleigh-Wave Theory and Application*, pp. 12–28, Springer, Berlin, Germany, 1985.

[6] V. Domarkas, B. T. Khuri-Yakub, and G. S. Kino, "Length and depth resonances of surface cracks and their use for crack size estimation," *Applied Physics Letters*, vol. 33, no. 7, pp. 557–559, 1978.

[7] S. Rokhlin and J. Kim, "In situ ultrasonic monitoring of surface fatigue crack initiation and growth from surface cavity," *International Journal of Fatigue*, vol. 25, no. 1, pp. 41–49, 2003.

[8] F. Hernandez-Valle, B. Dutton, and R. S. Edwards, "Laser ultrasonic characterisation of branched surface-breaking defects," *NDT & E International*, vol. 68, pp. 113–119, 2014.

[9] G. S. Kino, "The application of reciprocity theory to scattering of acoustic waves by flaws," *Journal of Applied Physics*, vol. 49, no. 6, pp. 3190–3199, 1978.

[10] B. A. Auld, "General electromechanical reciprocity relations applied to the calculation of elastic wave scattering coefficients," *Wave Motion*, vol. 1, no. 1, pp. 3–10, 1979.

[11] J. D. Achenbach and A. K. Gautesen, "Geometrical theory of diffraction for three-D elastodynamics," *The Journal of the Acoustical Society of America*, vol. 61, no. 2, pp. 413–421, 1977.

[12] C. Valle, M. Niethammer, J. Qu, and L. J. Jacobs, "Crack characterization using guided circumferential waves," *The Journal of the Acoustical Society of America*, vol. 110, no. 3, pp. 1282–1290, 2001.

[13] M. H. Rosli, R. S. Edwards, and Y. Fan, "In-plane and out-of-plane measurements of Rayleigh waves using EMATs for characterising surface cracks," *NDT & E International*, vol. 49, pp. 1–9, 2012.

[14] E. G. Straser and A. S. Kiremidjian, *A Modular, Wireless Damage Monitoring System for Structures*, John A. Blume Earthquake Engineering Center, Stanford, CA, USA, 1998.

[15] B. F. Spencer, M. E. Ruiz-Sandoval, and N. Kurata, "Smart sensing technology: opportunities and challenges," *Structural Control and Health Monitoring*, vol. 11, no. 4, pp. 349–368, 2004.

[16] M. B. Kane, *Wirelessly Enabled Control of Cyber-Physical Infrastructure with Applications to Hydronic Systems*, University of Michigan, Ann Arbor, MI, USA, 2014.

[17] S. Chen, X. Dong, J.-Y. Kim, S. Wu, and Y. Wang, "Design and performance validation of a compact wireless ultrasonic device for localized damage detection," *Advances in Structural Engineering*, vol. 19, no. 2, pp. 270–282, 2016.

[18] A. Pertsch, *An Intelligent Stand-Alone Ultrasonic Device for Monitoring Local Damage Growth in Civil Structures*, Georgia Institute of Technology, Atlanta, GA, USA, 2009.

[19] H. Yang, L. Guo, M. Zhan, and Z. Sun, "Research on the influence of material properties on cold ring rolling processes by 3D-FE numerical simulation," *Journal of Materials Processing Technology*, vol. 177, no. 1–3, pp. 634–638, 2006.

[20] ASM International, *ASM Handbook—Properties and Selection: Irons, Steels, and High Performance Alloys*, vol. 1, ASM International, Cleveland, OH, USA, 1990.

[21] J. Achenbach, *Wave Propagation in Elastic Solids*, North Holland Publishing Co., Amsterdam, Netherlands, 1973.

[22] D. T. Zeitvogel, K. H. Matlack, J.-Y. Kim, L. J. Jacobs, P. M. Singh, and J. Qu, "Characterization of stress corrosion cracking in carbon steel using nonlinear Rayleigh surface waves," *NDT & E International*, vol. 62, pp. 144–152, 2014.

[23] S. C. Hunter, "Energy absorbed by elastic waves during impact," *Journal of the Mechanics and Physics of Solids*, vol. 5, no. 3, pp. 162–171, 1957.

[24] B. E. Treeby, J. Jaros, A. P. Rendell, and B. T. Cox, "Modeling nonlinear ultrasound propagation in heterogeneous media with power law absorption using a k-space pseudospectral method," *The Journal of the Acoustical Society of America*, vol. 131, no. 6, pp. 4324–4336, 2012.

[25] S. J. Mirahmadi and F. Honarvar, "Application of signal processing techniques to ultrasonic testing of plates by S0 Lamb wave mode," *NDT & E International*, vol. 44, no. 1, pp. 131–137, 2011.

[26] S. Valliappan and V. Murti, *Finite Element Constraints in the Analysis of Wave Propagation Problems*, University of New South Wales, Sydney, Australia, 1984.

[27] M. Zhao, X. Du, J. Liu, and H. Liu, "Explicit finite element artificial boundary scheme for transient scalar waves in two-dimensional unbounded waveguide," *International Journal for Numerical Methods in Engineering*, vol. 87, no. 11, pp. 1074–1104, 2011.

[28] A. J. Deeks and M. F. Randolph, "Axisymmetric time-domain transmitting boundaries," *Journal of Engineering Mechanics*, vol. 120, no. 1, pp. 25–42, 1994.

[29] J. Liu and Y. Lu, "A direct method for analysis of dynamic soil-structure interaction based on interface idea," *Developments in Geotechnical Engineering*, vol. 83, no. 3, pp. 261–276, 1998.

[30] X. Dong, S. Chen, D. Zhu et al., "High-speed heterogeneous data acquisition using Martlet: a next-generation wireless sensing node," in *Proceedings of 6th World Conference on Structural Control and Monitoring*, European Association for the Control of Structures, Barcelona, Spain, pp. VS213–VS224, July 2014.

[31] H. Nyquist, "Certain topics in telegraph transmission theory," *Transactions of the American Institute of Electrical Engineers*, vol. 47, no. 2, pp. 617–644, 1928.

[32] C. E. Shannon, "A mathematical theory of communication," *Bell System Technical Journal*, vol. 27, no. 3, pp. 379–423, 1948.

[33] L. Yaroslavsky, *Fast Discrete Sinc-Interpolation: A Gold Standard for Image Resampling*, Hindawi Publishing Corporation, London, UK, 2007.

[34] A. Pertsch, J. Y. Kim, Y. Wang et al., "An intelligent stand-alone ultrasonic device for monitoring local structural damage: implementation and preliminary experiments," *Smart Materials and Structures*, vol. 20, no. 1, pp. 1–25, 2011.

[35] J.-Y. Kim and S. I. Rokhlin, "Surface acoustic wave measurements of small fatigue cracks initiated from a surface cavity," *International Journal of Solids and Structures*, vol. 39, no. 6, pp. 1487–1504, 2002.

[36] S. Foti, *Multistation Methods for Geotechnical Characterization Using Surface Waves*, Polytechnic University of Turin, Turin, Italy, 2000.

[37] F. Zhang, Y. F. Gao, Y. X. Wu, and N. Zhang, "Upper-bound solutions for face stability of circular tunnels in undrained clays," *Géotechnique*, vol. 68, no. 1, pp. 76–85, 2018.

[38] W. Liu, Y. Cho, H. Phan, and J. D. Achenbach, "Study on the scattering of 2-D Rayleigh waves by a cavity based on BEM simulation," *Journal of Mechanical Science and Technology*, vol. 25, no. 3, pp. 797–802, 2011.

[39] D. G. Aggelis, T. Shiotani, and D. Polyzos, "Characterization of surface crack depth and repair evaluation using Rayleigh waves," *Cement and Concrete Composites*, vol. 31, no. 1, pp. 77–83, 2009.

[40] W.-J. Song, J. S. Popovics, J. C. Aldrin, and S. P. Shah, "Measurement of surface wave transmission coefficient across surface-breaking cracks and notches in concrete," *The Journal of the Acoustical Society of America*, vol. 113, no. 2, pp. 717–725, 2003.

[41] G. Hévin, O. Abraham, H. A. Pedersen, and M. Campillo, "Characterization of surface cracks with Rayleigh waves: a numerical model," *NDT & E International*, vol. 31, no. 4, pp. 289–297, 1998.

[42] Y. C. Angel and J. D. Achenbach, "Reflection and transmission of obliquely incident Rayleigh waves by a surface-breaking crack," *The Journal of the Acoustical Society of America*, vol. 75, no. 2, pp. 313–319, 1984.